Journal of
Materials Chemistry C

COMMUNICATION

View Article Online
View Journal | View Issue

Cite this: *J. Mater. Chem. C*, 2015, 3, 8294

Received 20th May 2015,
Accepted 5th July 2015

DOI: 10.1039/c5tc01443c

www.rsc.org/MaterialsC

Reliable doping and carrier concentration control in graphene by aerosol-derived metal nanoparticles

Jong-Kwon Lee,[a] Hyangki Sung,[ab] Min Seok Jang,[a] Heetae Yoon[ab] and Mansoo Choi*[ab]

Reliable doping and carrier concentration control in graphene have been realized by depositing aerosol-derived metal nanoparticles (NPs) with consistent size and configuration on the channel of a graphene field-effect transistor. Here, the spherically shaped Ag or Pt NPs with a fairly narrow size distribution of 7.5 ± 1.5 or 6.4 ± 1.4 nm, respectively, have been produced through the spark discharge process. The transfer characteristics show that Ag NPs deposited on graphene induce n-type conduction with an electron concentration of 0.3–1.9 × 10^{12} cm^{-2} at a NP surface coverage of 12–21%, while Pt NPs lead p-type doping with a hole concentration of 3.9–5.2 × 10^{12} cm^{-2} at 24–32% surface coverage. The observed electrical transport properties are interpreted as the metal NP doping-induced Fermi level shift of initially p-type doped graphene by the adsorbed oxygen molecules under ambient conditions. Also, the minimum conductance at the Dirac point before and after the deposition of metal NPs shows no appreciable change, implying the absence of noticeable sp^3 hybridization of the graphene surface due to aerosol-derived NPs.

Introduction

Graphene, a two-dimensional hexagonal lattice of sp^2 hybridized carbon atoms, has attracted widespread interest due to its superior electrical, optical, chemical, and thermomechanical properties.[1–3] For the practical use of graphene in various fields such as electronics, photonics, energy, and catalysis, graphene doping is of great technological importance because it can tailor the electronic properties and chemical reactivity of graphene.[4–9] In previous studies, carrier doping control and p–n junction construction of graphene have been demonstrated mainly *via* electrostatic gating and chemical treatment.[10–15] However, the electrostatic gating typically requires a constant high electric field applied between the gate electrode and graphene which is undesirable for certain applications, while chemical doping exhibits little tunability and introduces defects into the lattice, reducing the carrier mobility.[16–18]

Recently, it has been theoretically predicted that a metal layer adsorbed on graphene can induce p- or n-type doping with various carrier concentration depending on the work function difference between the metal and graphene, as well as their equilibrium separation.[19] Then, several experimental reports have demonstrated doping control of graphene by thermally evaporated thin metal films.[20–23] However, it is difficult to control graphene-metal equilibrium separation by this metal layer deposition because a slight variation in deposition thickness significantly changes the surface morphology of the metal layer. For example, the isolated Al nanoparticles (NPs) formed with 0.5 nm thickness have insignificant contact area with graphene to achieve the appropriate doping effect, whereas Al NPs formed with 1.0 nm thickness start to coalesce towards continuous film turning the graphene into a metal.[21] A recent investigation has also reported that the configuration of the Au layer causes a change of doping type: n-type for Au NPs and p-type for the Au thin film.[24] These results are explained by the interplay between the work-function-difference induced electron transfer and the chemical-interaction induced potential variation due to the change in the surface morphology of a metal layer.[24] Meanwhile, metal NPs coated on graphene by the solution process always tend to form aggregates with spatially nonuniform distribution.[25] Thus, the random aggregation and island formation of metal NPs or thin metal films, occurred in a solution process or a thermal evaporator, make it hard to modulate carrier doping of graphene in a precisely controlled manner.

To achieve reliable doping and carrier concentration control of graphene, in this paper we report a new metal-graphene contact approach using aerosol-derived metal NPs. Unlike the conventional thermal evaporation method, the aerosol process enables a spatially uniform distribution of metal NPs with consistent size and shape, as well as less damage to the underlying graphene because of relatively low kinetic energy (KE) of metal NPs impinging on the surface of graphene. The electrical

---

[a] *Global Frontier Center for Multiscale Energy System, Seoul National University, Seoul 151-744, Republic of Korea. E-mail: mchoi@snu.ac.kr*

[b] *School of Mechanical and Aerospace Engineering, Seoul Natinoal University, Seoul 151-744, Republic of Korea*

transport measurements in an air ambient at room temperature show that Ag NPs with a surface coverage of 12–21% on graphene cause a shift in the Fermi energy (E_F) in graphene from the valence band through the Dirac point to the conduction band, inducing an electron concentration of 0.3–1.9 × 10^{12} cm^{-2}. Meanwhile, Pt NPs with a surface coverage of 24–32% cause a shift further into the valence band, resulting in a hole concentration of 3.9–5.2 × 10^{12} cm^{-2}. The observed transport properties of graphene deposited by metal NPs are explained in terms of metal induced E_F shift taking into account the initial adsorption of oxygen molecules on graphene under ambient conditions.

Experimental section

Fabrication of graphene field-effect transistors

The back-gated graphene field-effect transistors (FETs) were fabricated on a highly p-doped Si substrate covered with a 300 nm thick layer of thermally grown SiO_2 as schematically shown in Fig. 1a. Single-layer graphene grown on a Cu foil *via* chemical vapor deposition was transferred on the SiO_2 layer and identified using micro-Raman spectroscopy with 514 nm excitation as shown in Fig. 1b. The G band at 1591 cm^{-1} and the 2D band at 2688 cm^{-1} are observed in the Raman spectrum, and the peak intensity ratio of the 2D band to the G band greater than 1 indicates the single-layer graphene.[26] The graphene channels with a width of 10 μm and a length of 10 μm were defined utilizing photolithography and subsequent reactive ion etching in an oxygen ambient environment. Then, the source–drain electrode region was patterned by the deposition of Ni (1 nm) and Pd/Au (90/100 nm) metal layers onto the photoresist pattern *via* electron beam evaporation, followed by a lift-off process. The top view image of the completed graphene FET from an optical microscope is shown in the inset of Fig. 1b.

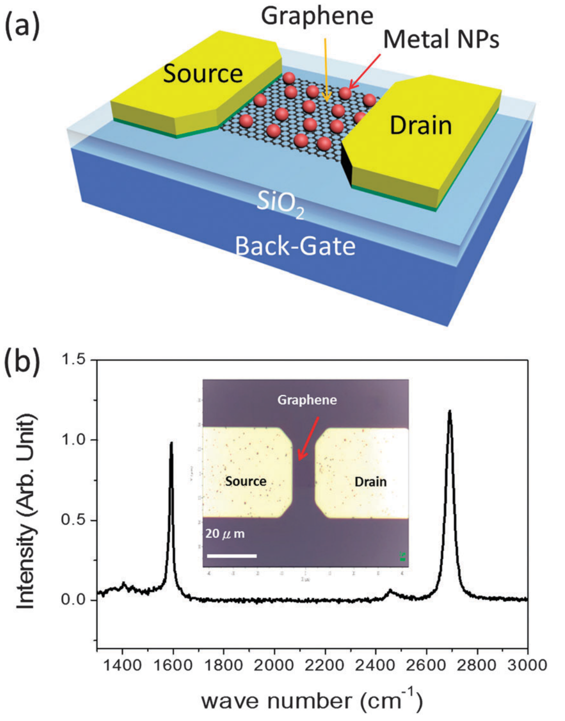

Fig. 1 (a) Schematic of the metal NP-deposited graphene field-effect transistor fabricated on the SiO_2/Si substrate. The electrical contacts are indicated as source, drain, and gate. (b) Raman spectrum (514 nm excitation) of a monolayer graphene film transferred on a SiO_2/Si substrate. The inset shows a top view image of the graphene channel and source/drain electrodes from an optical microscope.

Metal nanoparticle deposition through the aerosol process

To deposit the aerosol-derived metal NPs,[27] we used a spark discharge generator (SDG) and an electrostatic precipitator (ESP) as shown in Fig. 2. The SDG consists of a cylindrical chamber (an inner diameter of 20 mm, a height of 37 mm), a pin electrode made of a Ag or Pt wire (a diameter of 1.0 mm, Sigma Aldrich), and a plate electrode made of a Ag or Pt foil (5 mm × 5 mm × 0.25 mm, Sigma Aldrich). The axis of the pin electrode was aligned with the center of the plate electrode at which an exit hole of 1 mm-diameter was formed. The tip of the pin electrode was placed 1 mm above the plate electrode. The Ag or Pt NPs generated by the spark discharge between the electrodes were bipolarly charged and delivered to the ESP through the exit hole by N_2 carrier gas with a flow rate of 2.0 L min^{-1} or 3.0 L min^{-1}, respectively. The generation of the Ag or Pt NPs in the SDG was controlled by changing the frequency and the energy of sparks generated between the pin and plate electrodes using a RC circuit composed of a positive high voltage power supply, a 2 nF capacitor, and a 20 MΩ resistor. The plate electrode was grounded, and the pin electrode was positively biased by 5.0 kV. The ESP was composed of a grounded cylindrical chamber (an inner diameter of 52 mm and a height of 47 mm), and a bottom electrode made of Cu connected to a negative high voltage power supply. A Si substrate

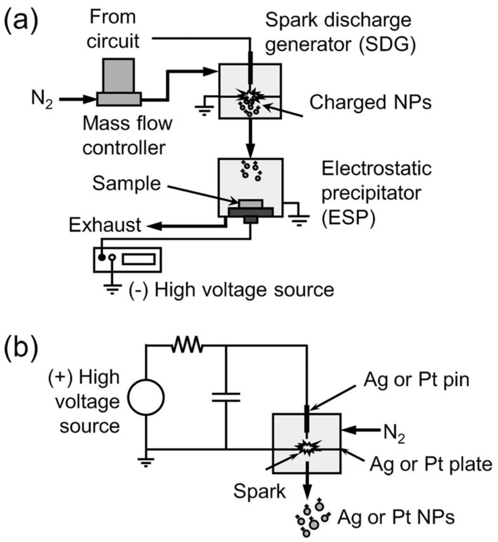

Fig. 2 (a) Schematic diagram of a spark discharge generator consisting of a pin and a plate electrode in a cylindrical chamber for controlling the metal NP generation, equipped with (b) an electrostatic precipitator system composed of a bottom electrode in a grounded cylindrical chamber for regulating the amount of carrier gas.

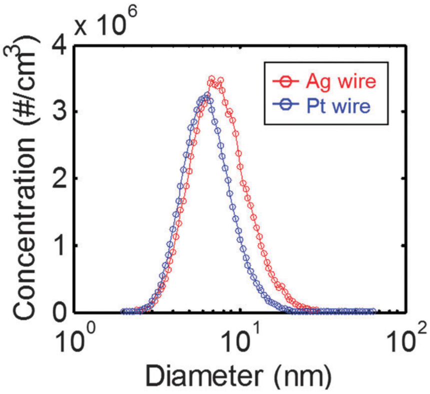

Fig. 3 Size distribution of aerosol-derived Ag and Pt NPs measured by the SMPS system. Geometrical mean diameters of Ag and Pt NPs are 7.5 and 6.4 nm, respectively, and the size of Ag NPs is distributed slightly broader than that of Pt NPs.

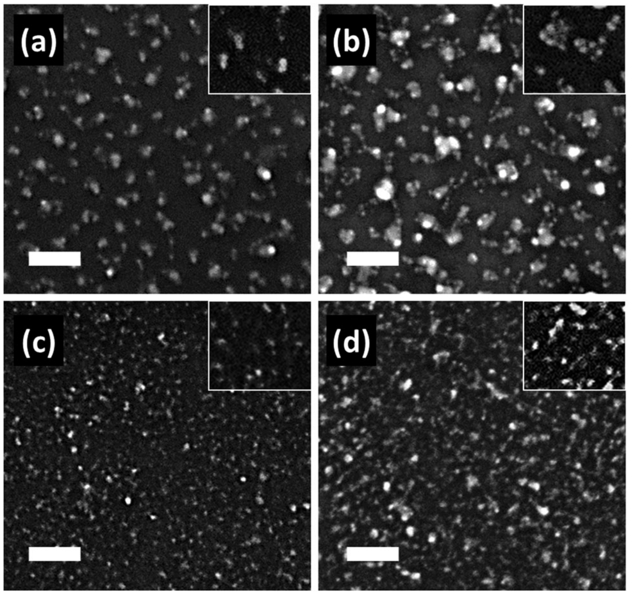

Fig. 4 FESEM images of the graphene channel deposited with different surface coverage of Ag NPs from (a) 12% to (b) 21% and Pt NPs from (c) 24% to (d) 32%, revealing uniformly distributed NPs with consistent size and shape. The scale bars in the images are 100 nm, and the insets represent 2-fold enlarged images.

with graphene field-effect transistors was placed on the bottom electrode in the ESP. The positively charged Ag or Pt NPs fed into the ESP were electrostatically guided to and deposited on the substrate surface as the bottom electrode was negatively biased. The magnitude of the negative potential at the bottom electrode was chosen to be −1.0 kV, which resulted in various particle densities on graphene films across a substrate in a single deposition by changing the deposition time.

The size distribution of the Ag and Pt NPs generated in the SDG was measured using a scanning mobility particle sizer (SMPS) system consisting of an electrostatic classifier (TSI 3080) with a Kr-85 radiative neutralizer, a differential mobility analyzer (TSI 3085), and a condensation nuclei counter (TSI 3776). The generated Ag NPs with a total concentration of 9.2×10^7 cm^{-3} have a geometrical mean diameter (d_g) of 7.5 nm and a standard deviation (σ_g) of 1.5 nm, whereas the Pt NPs with a concentration of 7.3×10^7 cm^{-3} have a d_g of 6.4 nm and a σ_g of 1.4 nm as shown in Fig. 3. Upon their generation in the SDG, the metal NPs were fed into the ESP and deposited on the graphene FET. The surface coverage derived by the ratio of the occupied area on average for metal NPs to the area of the graphene channel was obtained from their scanning electron microscope (SEM) images. The surface coverage of Ag NPs uniformly deposited on the graphene channels ranges from 12 (Fig. 4a), 16, 18 to 21% (Fig. 4b), while that of Pt NPs ranges from 24 (Fig. 4c), 26, 29 to 32% (Fig. 4d). The insets in Fig. 4, 2-fold enlarged SEM images, demonstrate that the spherical metal NPs are well dispersed with consistent configuration, although the NPs appear to be slightly agglomerated with increasing surface coverage.

Results and discussion

Graphene FETs deposited by aerosol-derived Ag or Pt NPs were investigated by transport measurements under ambient conditions to observe the shift of the Dirac point, the gate voltage of minimum conductivity, depending on electron or hole doping levels.[8,22] Here, a constant drain–source voltage (V_{DS}) of 0.01 V was applied to the graphene FET, and the drain–source current (I_{DS}) as a function of the gate-source voltage (V_{GS}) in a range of −60 V to 100 V was measured by using an Agilent 4154C semiconductor parameter analyzer at room temperature. Fig. 5 shows the transport properties of the fabricated graphene FETs before and after the deposition of metal NPs. Before metal NP deposition on the graphene channel, the Dirac point of ∼22 V in initial graphene exhibits a p-type doping arising from the adsorption of oxygen molecules in air and the underlying SiO_2 layer.[5,28,29] When the graphene channel is deposited with Ag or Pt NPs, the smaller workfunction (W_F) of Ag (∼4.24 eV) or the larger W_F of Pt (∼5.9 eV)[30] than that of graphene (∼4.89 eV)[31] induces the transfer of electrons from Ag NPs to graphene or from graphene to Pt NPs, resulting in an upward or a downward shift in the E_F of graphene, respectively. Such an upward or a downward shift in the E_F level makes graphene effectively n-type or p-type doped. As the surface coverage of Ag NPs increases from 12, 16, 18 to 21%, the Dirac point in graphene is shifted towards the negative V_{GS} from 18, 9, 3 to −4 V, respectively, as shown in Fig. 5a. Meanwhile, as the surface coverage of Pt NPs increases from 24, 26, 29 to 32%, the Dirac point in graphene is shifted towards higher positive V_{GS} from 76, 80, 89 to 93 V, respectively, as shown in Fig. 5b.

According to the shift of the Dirac point, the carrier density of graphene induced by the deposition of metal NPs is estimated from the relation as

$$\Delta n = \frac{C_G}{e}(\Delta V_{Dirac}) \tag{1}$$

where C_G is the gate capacitance per unit area, e is the electric charge, Δn is a net carrier concentration, and ΔV_{Dirac} is a shift of

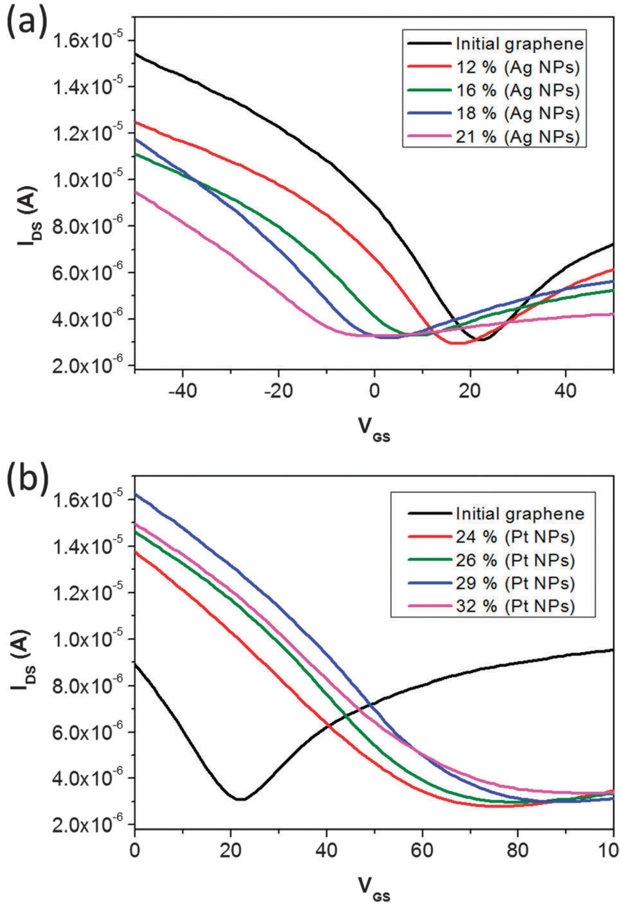

Fig. 5 Transfer characteristics of graphene FETs with and without (a) Ag NP deposition and (b) Pt NP deposition. Ag NPs on graphene cause a shift in the Dirac point in the negative gate bias direction, while Pt NPs cause a shift in the positive gate bias direction.

the Dirac point in metal NP-deposited graphene relative to that in the initially p-type doped graphene ($V^0_{\mathrm{Dirac}} \sim 22$ V). The initial hole doping concentration of graphene due to adsorbed oxygen molecules is estimated to be 1.6×10^{12} cm^{-2}. Here it is noted that the plus (minus) value indicates a concentration of hole (electron) carriers. When the surface coverage of Ag NPs increases from 12, 16, 18 to 21%, $\Delta V_{\mathrm{Dirac}}$ of −4, −13, −19 to −26 V in the Ag NP-deposited graphenes corresponds to a net electron concentration of -2.9×10^{11}, -9.5×10^{11}, -1.4×10^{12} to -1.9×10^{12} cm^{-2}, respectively. Meanwhile, when the surface coverage of Pt NPs increases from 24, 26, 29 to 32%, $\Delta V_{\mathrm{Dirac}}$ of 54, 58, 67 to 71 V in the Pt NP-deposited graphenes leads to a net hole concentration of 3.9×10^{12}, 4.2×10^{12}, 4.9×10^{12} to 5.2×10^{12} cm^{-2}, respectively. Graphs to correlate the doping concentration with the surface coverage, or interparticle spacing, of metal NPs are shown in Fig. 6. These results demonstrate that our metal-graphene contact approach allows us to modulate the doping level of graphene by precisely controlling the surface coverage, or interparticle spacing, with consistent configuration, while the previously reported solution or thermal evaporation processes suffer from random aggregation or island formation issues.

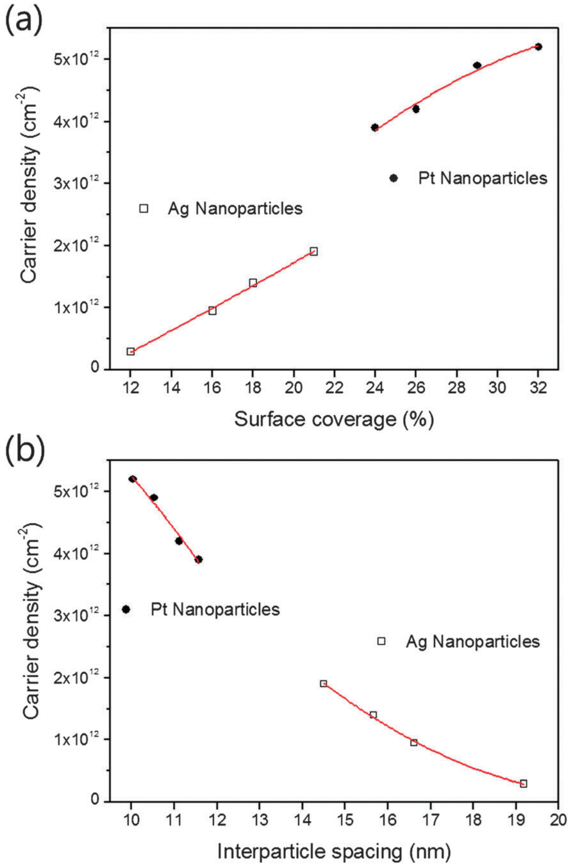

Fig. 6 Carrier density of graphene as a function of (a) the surface coverage or (b) the interparticle spacing for Ag and Pt NPs: the open squares and the closed black circles correspond to Ag and Pt NPs deposited on graphene, respectively, while the solid red lines are the fit curves.

To analyse the electrical transport characteristics of metal NP-doped graphene in an air ambient at room temperature, we depicted the schematic energy band diagrams of graphenes deposited by Ag NPs and Pt NPs as shown in Fig. 7a and b. The E_{F} of initial graphene before the deposition of metal NPs is situated on a valance band (black Dirac cone) because of the oxygen molecules adsorbed on the graphene channel. As the surface coverage of Ag NPs deposited on this graphene increases from 12, 16, 18 to 21%, E_{F} of the graphene is shifted upward to the Dirac point (red, green, blue Dirac cones) and then further moved to the conduction band (pink Dirac cone) doped with n-type as shown in Fig. 7a. When we apply a gate voltage (V_{GS}) in the negative direction less than each Dirac point, *e.g.* at $V_{\mathrm{GS}} = -20$ V, the graphene sheets before and after the deposition of Ag NPs are electrostatically doped to strong p- and p-type with the E_{F} situated in the valence band, increasing hole currents. Thus, the hole current in the Ag-doped graphene channels is lower than that of initial graphene as shown in Fig. 5a. Meanwhile, as we increase the V_{GS} in the positive direction, the E_{F} is shifted upward to the conduction band passing through the Dirac point. As a result, the graphene channels before and after Ag NP deposition are expected to be n- and strong n-type with the E_{F} located in the conduction band,

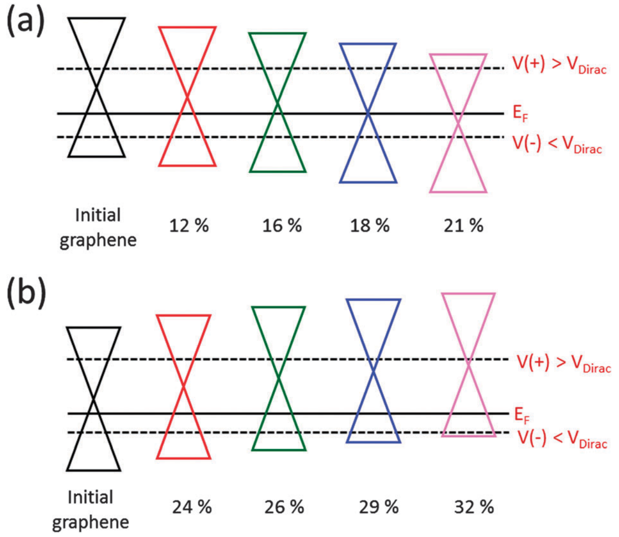

Fig. 7 Schematic energy band diagrams of graphenes before and after (a) Ag NPs doping with different surface coverage of 12, 16, 18, and 21%, and (b) Pt NPs doping with 24, 26, 29 and 32%.

dominated by the electron transport. However, the absorbed oxygen molecules on graphene act as electron acceptors and become negatively charged impurities,[32] whereas Ag NPs on graphene induce n-type doping. These charged impurities may reduce the electron mobility of graphene through typical charged impurity scattering.[33] Thus, as the V_{GS} changes in a positive voltage range, the electron current in Ag-deposited graphene becomes higher or lower than that in graphene without NPs depending on the interrelation between the variation of carrier concentration and the decrease in carrier mobility.

On the other hand, as the surface coverage of Pt NPs deposited on the graphene increases from 24, 26, 29 to 32%, the E_F of the graphene is shifted downward to the valance band region (red, green, blue, and pink Dirac cones) doped with p-type as shown in Fig. 7b. At a V_{GS} in the negative direction less than each Dirac point, the graphenes before and after the deposition of Pt NPs are electrostatically doped to p- and strong p-type dominated by hole current through the channels, resulting in higher hole current in Pt-doped graphene than the initial graphene, *e.g.* at V_{GS} = 10 V, as demonstrated in Fig. 5b. As we apply the V_{GS} in the positive direction, the E_F in the graphene channels is shifted upward to the conduction band passing through each Dirac point. When the E_F meets the Dirac point, the reduced density of states in the graphene channel leads to minimum conductance. At a positive V_G greater than each V_{Dirac}, the graphenes before and after the Pt NP deposition are electrostatically doped to strong n- and n-type, respectively, dominated by electron current. Here, the weak n-type conduction in the Pt-doped graphene compared to the strong n+-type initial graphene leads to the suppression of electron currents in this positive gate voltage range. Additionally, the charge impurity scattering by the oxygen molecules initially adsorbed on graphene may lower the electron mobility of graphene. Thus, as the surface coverage of Pt NPs increases, a strong p-type doping in graphene is enhanced, and consequently the bipolar characteristics of graphene become unipolar ones as shown in Fig. 5b.

It is noted that the consistent surface morphology of aerosol-derived metal NPs allows us to interpret the change in the doping level of graphene by the work function-difference induced electron transfer between the metal NPs and graphene. Meanwhile, the uncontrollable graphene-metal equilibrium separation due to the random morphologies of thermally deposited metal layers or spin-coated metal NPs causes a chemical-interaction induced potential variation, which makes it hard to precisely modulate the carrier concentration of graphene. Moreover, it is observed that graphene deposited by aerosol-derived metal NPs does not show any appreciable change in the conductance at the Dirac point, indicating an absence of transition from in-plane sp^2 hybridization to off-plane sp^3 hybridization of the graphene surface[34,35] due to metal NP-induced local defects. According to the previous reports, the bond dissociation energy of C–N and C–C (sp^3–sp^2) covalent bonds is typically in order of 3–4 eV,[36] and van der Waals bond energy of carbon layers amounts usually to a few tenths of eV.[37] Since the KE of thermally evaporated nanoparticles determined by the process temperature is an order of a few tenth eV, they can cause damage to the van der Waals bond underlying graphene layers. Meanwhile, the KE of aerosol-derived metal NPs with an impinging velocity, determined by balancing the electrostatic and fluid frictional forces, is estimated to be a few meV, expecting no significant damage to the underlying graphene layers.[38] In this respect, the aerosol-derived metal NPs with consistent size and configuration can afford reliable control in carrier concentration to modulate electrical transport properties of graphene with no appreciable impact on a graphene surface, compared to the previously reported methods. Therefore, the suggested metal-graphene contact approach can be regarded as an effective way of tailoring electronic properties and chemical reactivity of graphene for versatile device applications.

Conclusions

Ag and Pt NPs with consistent size and shape generated by the aerosol process have been used for reliable doping and carrier concentration control in graphene under ambient conditions. Ag NPs with a surface coverage of 21% induce an electron concentration of 1.9×10^{12} cm^{-2}, whereas Pt NPs with a surface coverage of 32% lead to a hole concentration of 5.1×10^{12} cm^{-2} for an initially p-doped graphene (1.6×10^{12} cm^{-2}) by the ambient oxygen molecules. Here the aerosol-derived metal NPs modulate electrical transport properties of graphene with no appreciable impact on the graphene surface compared to the previous methods. Thus, aerosol-derived metal NP deposition on graphene can be an efficient approach to precisely tailor the electronic properties and chemical reactivity of graphene.

Acknowledgements

This work was supported by the Global Frontier R&D Program on Center for Multiscale Energy System (Grant No. 2011-0031561 and 2012M3A6A7054855) funded by the National Research Foundation under the Ministry of Science, ICT, and Future Planning, Korea. M. S. J. gratefully acknowledges a post-doctoral fellowship from the POSCO TJ Park Foundation.

Notes and references

1 A. K. Geim, *Science*, 2009, **324**, 1530.

2 Y. Zhu, S. Murali, W. Cai, X. Li, J. W. Suk, J. R. Potts and R. S. Ruoff, *Adv. Mater.*, 2010, **22**, 3906.

3 W. Bao, F. Miao, Z. Chen, H. Zhang, W. Jang, C. Dames and C. N. Lau, *Nat. Nanotechnol.*, 2009, **4**, 562.

4 H. Li, Q. Zhang, C. Liu, S. Xu and P. Gao, *ACS Nano*, 2011, **5**, 3198.

5 P. Joshi, H. E. Romero, A. T. Neal, V. K. Toutam and S. A. Tadigadapa, *J. Phys.: Condens. Matter*, 2010, **22**, 334214.

6 Y. Shao, S. Zhang, M. H. Engelhard, G. Li, G. Shao, Y. Wang, J. Liu, I. A. Aksay and Y. Lin, *J. Mater. Chem.*, 2010, **20**, 7491.

7 Z. Yan, J. Yao, Z. Sun, Y. Zhu and J. M. Tour, *Small*, 2012, **8**, 59.

8 A. Das, S. Pisana, B. Chakraborty, S. Piscanec, S. K. Saha, U. V. Waghmare, K. S. Novoselov, H. R. Krishnamurthy, A. K. Geim, A. C. Ferrari and A. K. Sood, *Nat. Nanotechnol.*, 2008, **3**, 210.

9 M. Pumera, *J. Mater. Chem. C*, 2014, **2**, 6454.

10 J. R. Williams, L. DiCarlo and C. M. Marcus, *Science*, 2007, **317**, 638.

11 B. Huard, J. A. Sulpizio, N. Stander, K. Todd, B. Yang and D. Goldhaber-Gordon, *Phys. Rev. Lett.*, 2007, **98**, 236803.

12 D. B. Farmer, R. Golizadeh-Mojarad, V. Perebeinos, Y.-M. Lin, G. S. Tulevski, J. C. Tsang and P. Avouris, *Nano Lett.*, 2009, **9**, 388.

13 T. Lohmann, K. v. Klitzing and J. H. Smet, *Nano Lett.*, 2009, **9**, 1973.

14 H. Liu, Y. Liu and D. Zhu, *J. Mater. Chem.*, 2011, **21**, 3335.

15 X. Miao, S. Tongay, M. K. Petterson, K. Berke, A. G. Rinzler, B. R. Appleton and A. F. Hebard, *Nano Lett.*, 2012, **12**, 2745.

16 D. Wei, Y. Liu, Y. Wang, H. Zhang, L. Huang and G. Yu, *Nano Lett.*, 2009, **9**, 1752.

17 Z. Sun, Z. Yan, J. Yao, E. Beitler, Y. Zhu and J. M. Tour, *Nature*, 2010, **468**, 549.

18 Y.-C. Lin, C.-Y. Lin and P.-W. Chiu, *Appl. Phys. Lett.*, 2010, **96**, 133110.

19 G. Giovannetti, P. A. Khomyakov, G. Brocks, V. M. Karpan, J. v. d. Brick and P. J. Kelly, *Phys. Rev. Lett.*, 2008, **101**, 026803.

20 W. X. Wang, S. H. Liang, T. Yu, D. H. Li, Y. B. Li and X. F. Han, *J. Appl. Phys.*, 2011, **109**, 07C501.

21 X. Shi, G. Dong, M. Fang, F. Wang, H. Lin, W.-C. Yen, K. S. Chan, Y.-L. Chueh and J. C. Ho, *J. Mater. Chem. C*, 2014, **2**, 5417.

22 Y. Ren, S. Chen, W. Cai, Y. Zhu, C. Zhu and R. S. Ruoff, *Appl. Phys. Lett.*, 2010, **97**, 053107.

23 J. Lee, K. S. Novoselov and H. S. Shin, *ACS Nano*, 2011, **5**, 608.

24 Y. Wu, W. Jiang, Y. Ren, W. Cai, W. H. Lee, H. Li, R. D. Piner, C. W. Pope, Y. Hao, H. Ji, J. Kang and R. S. Ruoff, *Small*, 2012, **8**, 3129.

25 R. Muszynski, B. Seger and P. V. Kamat, *J. Phys. Chem. C*, 2008, **112**, 5263.

26 A. C. Ferrari, *Solid State Commun.*, 2007, **143**, 47.

27 K. Han, W. Kim, J. Yu, J. Lee, H. Lee, C. Gyu Woo and M. Choi, *J. Aerosol Sci.*, 2012, **52**, 80.

28 S. Ryu, L. Liu, S. Berciaud, Y.-J. Yu, H. Liu, P. Kim, G. W. Flynn and L. E. Brus, *Nano Lett.*, 2010, **10**, 4944.

29 Y.-J. Kang, J. Kang and K. J. Chang, *Phys. Rev. B*, 2008, **78**, 115404.

30 *CRC Handbook of Chemistry and Physics*, CRC press, 2008, vol. 30.

31 S. M. Song, J. K. Park, O. J. Sul and B. J. Cho, *Nano Lett.*, 2012, **12**, 3887.

32 B. Chen, H. Huang, X. Ma, L. Huang, Z. Zhang and L.-M. Peng, *Nanoscale*, 2014, **6**, 15255.

33 J.-H. Chen, C. Jang, S. Adam, M. S. Fuhrer, E. D. Williams and M. Ishigami, *Nat. Phys.*, 2008, **4**, 377.

34 S. H. Al-Harthi, M. Elzain, M. Al-Barwani, A. Kora'a, T. Hysen, M. T. Z. Myint and M. R. Anantharaman, *Nanoscale Res. Lett.*, 2012, **7**, 466.

35 M. Lafkioti, B. Krauss, T. Lohmann, U. Zschieschang, H. Klauk, K. v. Klitzing and J. H. Smet, *Nano Lett.*, 2010, **10**, 1149.

36 D. Y. Kondakov, *J. Appl. Phys.*, 2008, **104**, 084520.

37 V. V. Gobre and A. Tkatchenko, *Nat. Commun.*, 2013, **4**, 2341.

38 H. Sung, J. Lee, K. Han, J.-K. Lee, J. Sung, D. Kim, M. Choi and C. Kim, *Org. Electron.*, 2014, **15**, 491.